Supporting Information

Colloidal Plasmonic Nanostar Antennas with Wide Range Resonance Tunability

Ted V. Tsoulos,[1] Supriya Atta,[2] Maureen J. Lagos,[1,3] Michael Beetz,[4] Philip E. Batson,[1,3] George Tsilomelekis,[5] and Laura Fabris*[1]

[1] Department of Materials Science and Engineering, Rutgers University, 607 Taylor Road Piscataway NJ 08854, United States.

[2] Department of Chemistry and Chemical Biology, Rutgers University, 610 Taylor Road Piscataway NJ 08854, United States.

[3]Department of Physics & Astronomy, Rutgers University, 136 Frelinghuysen Road, Piscataway NJ 08854.

[4] Department of Chemistry and Center for NanoScience (CeNS), Ludwig Maximilians Universität München, 81377 Munich, Germany.

[5] Department of Chemical and Biochemical Engineering, Rutgers University, 98 Brett Road, Piscataway NJ 08854, United States.

Modeling

Using a linearly polarized (LP) incident light source, as seen in **Equation 1**, with an electric field of amplitude 1 V/m, we simulated the optical properties of nanostars using a model developed in the RF Module of COMSOL Multiphysics 5.0.

1) $$\boldsymbol{E} = e^{-j\boldsymbol{k_0 z}}\,\hat{x}$$

The simulations were based on numerical solutions of a time-averaged Laplacian, seen in **Equation 2**, employing the widely used Finite Element Method.

(2) $$\nabla \times \frac{1}{\mu_r}(\nabla \times \boldsymbol{E}) - {k_0}^2\left(\varepsilon_r - \frac{j\sigma}{\omega\varepsilon_0}\right)\boldsymbol{E} = \boldsymbol{0}$$

The geometry was built on three concentric domains. A fully absorbing spherical layer, usually referred to as perfectly matched layer (PML), a layer assigned the dielectric properties of water, from Hale and Querry,[1] and a core domain including the various nanostar models assigned the dielectric properties of gold from the Lorentz–Drude model by Johnson and Christy.[2] The relative permeability μ_r was taken to be 1 in all geometry domains without loss of generality. The angular frequency ω was calculated from the input wavelength values.

The nanostar models were also developed in Comsol Multiphysics using mostly a spherical core, eccentric conical spikes with hemispherical, oblate, and prolate hemiellipsoidal tips. The volume and surface areas of these models are defined by **Equations 3** and **4** with *i* being the number of spikes, varying from 1 to 6 in this work.

(3) $$V = \frac{4}{3}\pi a^3 + \sum_{i=1}^{n}\left\{\frac{h_i}{3}\pi(R_i^2 + R_i r_i + r_i^2) + \frac{2}{3}\pi r_i^3 - \frac{\pi}{6}\left(a - \sqrt{a^2 - R_i^2}\right)\left[3R_i^2 + (a - \sqrt{a^2 - R_i^2})^2\right]\right\}$$

(4) $$A = 4\pi a^2 - \sum_{i=1}^{n}\left\{2\pi a\,(a - \sqrt{a^2 - {R_i}^2}\right\} + \sum_{i=1}^{n}\left\{\pi\,(r_i + R_i)\sqrt{(R_i - r_i)^2 + {h_i}^2} + 2\pi {r_i}^2\right\}$$

Furthermore, *a* is the radius of the spherical core, *R* is the base radius of a spike, *r* is the radius of the hemispherical tip of a spike, and *h* is the distance between *R* and *r*. Note that these equations describe only the cases of nanostars with hemispherical tips.

The various nanostar models were built to match the shapes and complexity of nanostars synthesized experimentally, and characterized *via* transmission electron microscopy (TEM), as described below. Herein, for sake of completeness, we compared the results collected *via* simulations to both those obtained on individual nanostars *via* electron energy loss spectroscopy (EELS) and to the ensemble averaged ones derived from the large-number statistical analysis of nanostar suspensions. Importantly, the excellent sample monodispersity and batch-to-batch reproducibility achievable with the synthetic protocol described herein, allow us to exactly match the plasmonic resonances observed experimentally to those calculated computationally, thus enabling us to identify additional resonant and coupling modes in these nanoparticles.

The layered geometry was meshed employing randomly distributed tetrahedra, whose size was kept between 0.1 and 2 nm within the NS domain and at less than 4 nm in the surrounding medium domain. Numerical solutions of Equation 2 were accomplished through an iterative method in which the difference between individual solutions in the constituent tetrahedral elements is minimized within a tolerance of 10^{-6}. The whole procedure is based on convergence of the individual solutions within the above tolerance.

From the solution of Equation 2, we provide plots of the normalized scattered electric field. Three dimensional plots of the electric field norm (**Equation 5**) on the surface of the various nanostars along with two-dimensional slice plots of the electric field norm are presented. 2D slice plots are fundamental to study, at the same time, surface and bulk plasmon modes in these nanoparticles.

(5) $$|\boldsymbol{E}| = \sqrt{{E_x}^2 + {E_y}^2 + {E_z}^2}$$

In parallel, we calculate the absorption, scattering, and extinction cross sections, as defined by **Equations 6** and **7**.

(6) $$\sigma_{abs} = \frac{\boldsymbol{W}_{abs}}{\boldsymbol{P}_{inc}} \qquad \sigma_{sca} = \frac{\boldsymbol{W}_{sca}}{\boldsymbol{P}_{inc}}$$

(7) $$\sigma_{ext} = \sigma_{abs} + \sigma_{sca}$$

The absorption and scattering cross sections are defined by the energy rates absorbed and scattered by the nanostar volume and surface area, defined in **Equations 8** and **9** respectively, and divided by the incident irradiance, given by **Equation 10**:

(8) $$\boldsymbol{W}_{abs} = \frac{1}{2}\iiint_{xyz} [\,\mathrm{Re}[(\sigma\mathbf{E} + j\omega\boldsymbol{D}) \cdot \mathbf{E}^*] + j\omega\boldsymbol{B}) \cdot \mathbf{H}^*]\ \mathrm{dxdydz}\ \ (\mathrm{W})$$

(9) $$\boldsymbol{W}_{sca} = \oiint [\boldsymbol{E} \times \boldsymbol{H}^*] \cdot \mathbf{n}\mathrm{dS}\ \ (\mathrm{W})$$

(10) $$\boldsymbol{P}_{inc} = \frac{1}{2Z_0}|\boldsymbol{E}_0|^2$$

where Z_0 is the impedance of free space and E_0 is the amplitude of the incident electric field, 1 V/m as seen in Equation 1**.**

Additionally, given the extinction cross section, we calculate the shape- and concentration-dependent extinction coefficient by multiplying the extinction cross section with the number density of nanostars as seen in **Equation 11**:

(11) $$\varepsilon_{dep} = \sigma_{ext}\, n$$

Similarly, the absorption coefficient is given by **Equation 12**.

(12) $$a = \sigma_{abs} n$$

This is a concentration dependent quantity, since it contains the number density of nanostars *n*. In this work, it is compared to the experimental absorption coefficient, obtained from the measured absorbance from **Equation 15.** We deduce **Equation 15** by combining **Equation 13**, the Beer-Lambert law, and the definition of absorption coefficient **Equation 14**, where Abs is the experimentally measured absorbance, I and I_0 the incident and transmitted light intensities, z the light path length through the cuvette holding the aqueous NS suspensions, and α_{exp} the experimental absorption coefficient.

(13) $$Abs = log_{10} \frac{I_0}{I}$$

(14) $$I = I_0 \, e^{-\alpha_{exp} z}$$

(15) $$\alpha_{exp} = \frac{\ln(10) Abs}{z}$$

The relationships described above allow us to directly compare the calculated absorption cross section spectra to the UV-Vis-NIR absorption spectra obtained experimentally, as in detail described in our previous work.[3]

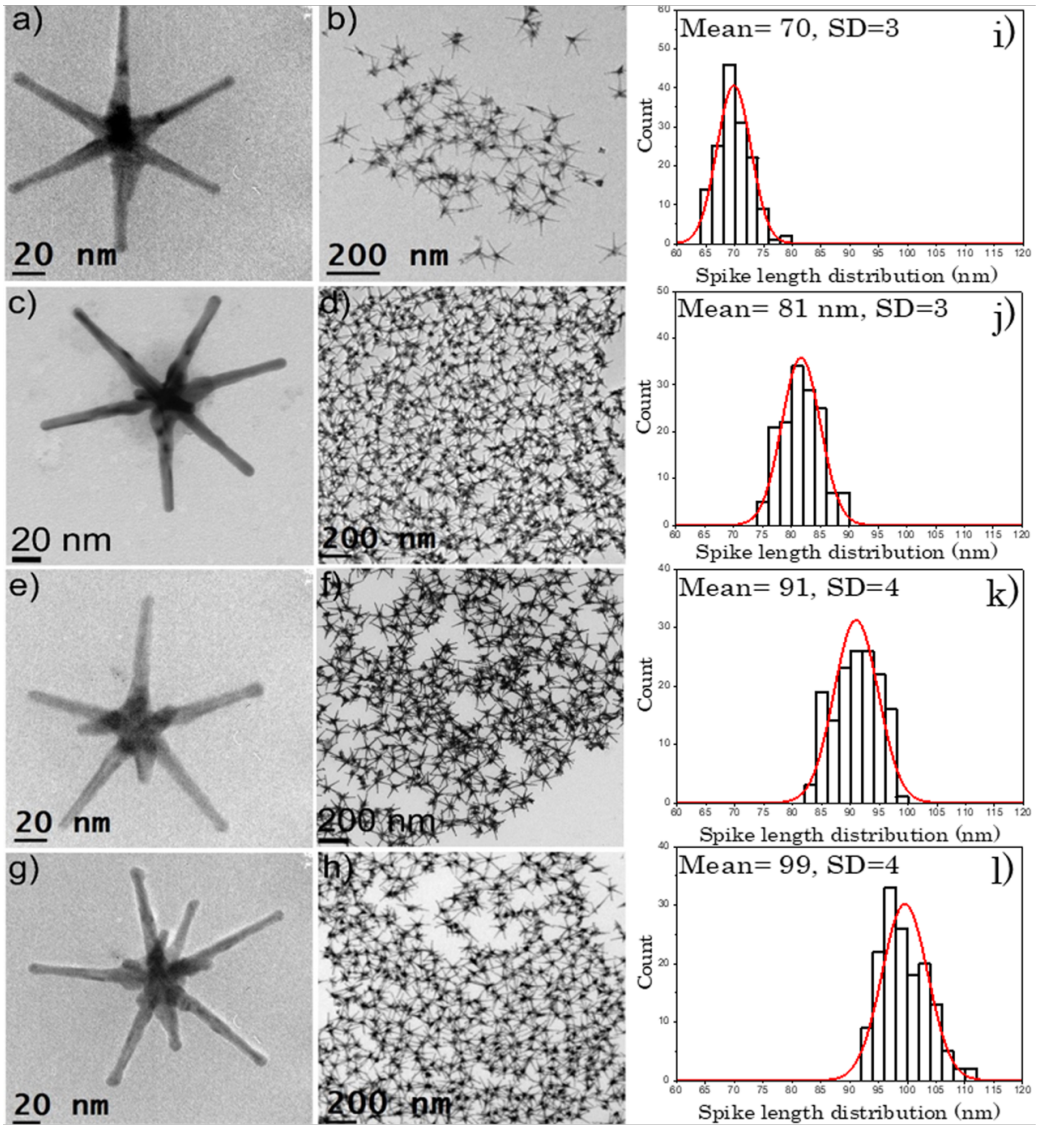

Figure S1. Representative transmission electron microscopy (TEM) micrographs of 6-branched gold nanostars in the order of increasing spike length (a, c, e, and g). These syntheses lead to monodispersed samples in high yield, as evidenced in the TEM micrographs (b, d, f, and h). Statistical analysis of the spike length distribution of 6-branched gold nanostars was obtained by measuring the length of 150 spikes from different areas on the TEM grid for each sample. Spike length analysis: i) Mean: 70 nm; Standard deviation: 3 nm, j) Mean: 81 nm; Standard deviation: 3 nm, k) Mean: 91 nm; Standard deviation: 4 nm, and l) Mean: 99 nm; Standard deviation: 4 nm. Bin size in i)-l): 2 nm. Gaussian curves obtained from full data sets.

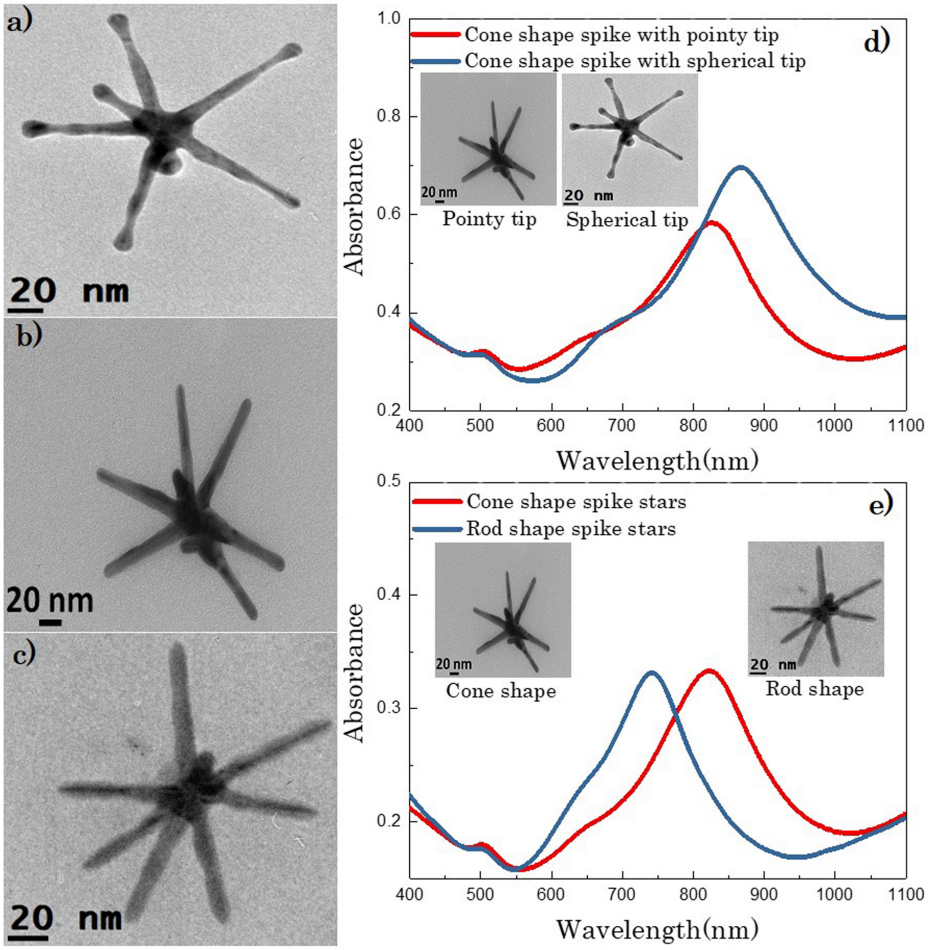

Figure S2. TEM micrographs and UV-Vis-NIR spectra of gold nanostars with different spike and tip shapes. In our syntheses we obtained two different spike morphologies, conical and rod-like. The conical tip morphology can also be obtained with two different tip morphologies, pointy and spherical. The experimental optical spectra of two different cone-shaped stars, with pointy and spherical tips, and two different types of stars, with conical and rod-shaped spikes are reported here. A blue shift from 824 nm to 867 nm of the LSPR was observed from the pointy tip to the spherical tip morphology respectively, while a blue shift of the LSPR by 83 nm was observed moving from the cone shape to the rod shape morphology.

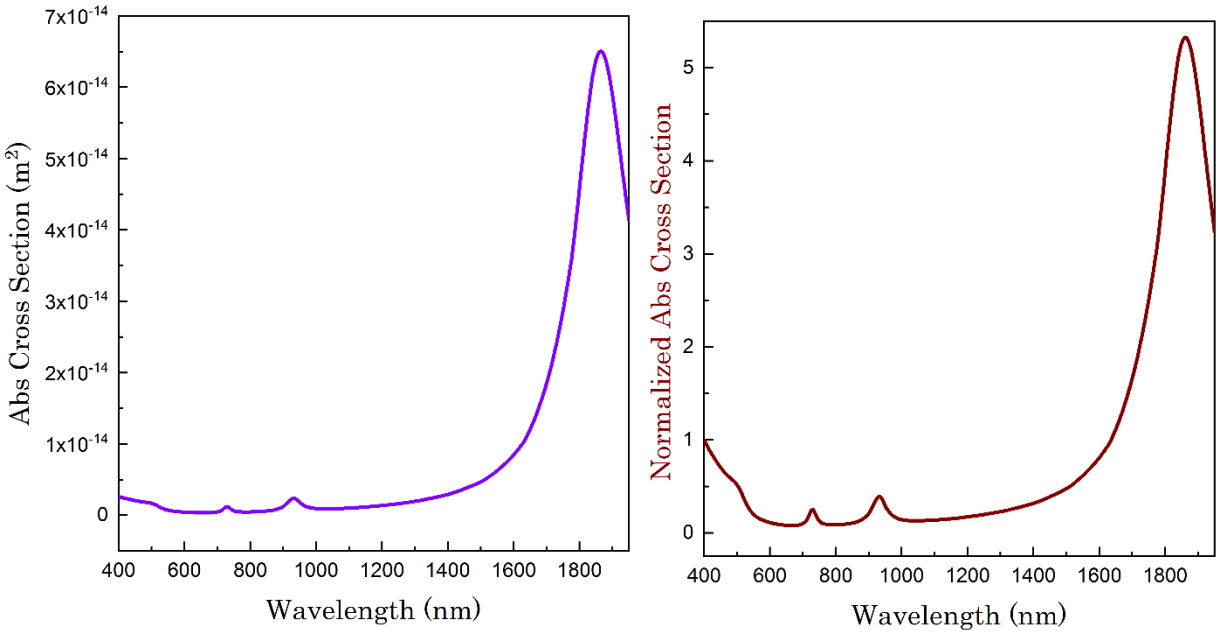

Figure S3: Comparison between the normalized absorption cross section spectrum (left, as presented in Figure 3e) in comparison to the full-range absorption cross section spectrum presented in Figure 3c. The normalization method consists of two steps. First, we divide the absorption cross section spectrum by the absorption cross section value at 400 nm. Second, we multiply the resulting values by the ratio between the photon energy at each wavelength and the photon energy of a 400 nm photon. As it can be observed, the relative peak intensities (normalized and not) do not change substantially, underscoring that the substantial intensity observed for the first harmonic mode is indeed an intrinsic property of the system studied.

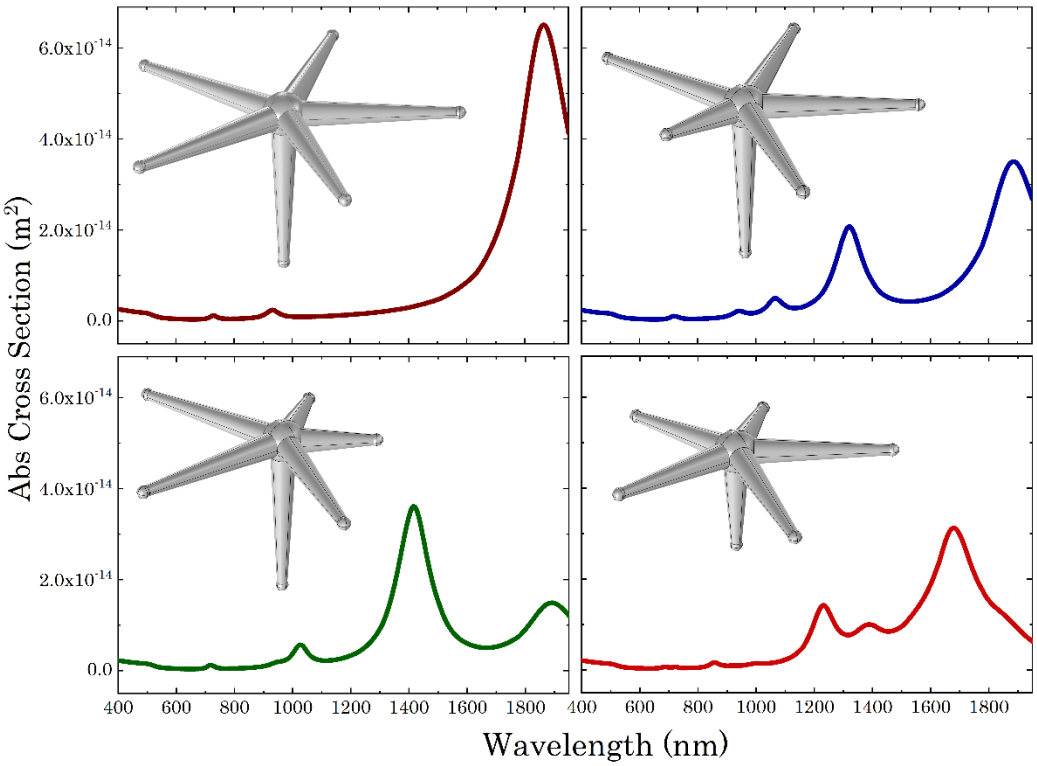

Figure S4: We demonstrate the shifts of the harmonics and additional hybrid resonances that arise when we introduce disruptions in the geometry of a 90 nm-spike gold nanostar. Starting by halving the length of one of the spikes, we elaborate by halving the length of two spikes, and end up with a nanostar with 6 spikes with different lengths. Clearly there are additional resonances appearing that correspond to shifted resonances of the shorter spikes and hybrid ones that correspond to mixed states, *e.g.* the second harmonic of one spike resonates with the third harmonic of another spike. It is important to note also that, contrary to the symmetric structure depicted in the first graph (as also presented in the main text), the 6th spike placed perpendicular to the five in-plane spikes participates with higher intensity to all of the resonances in all of the three disrupted cases presented.

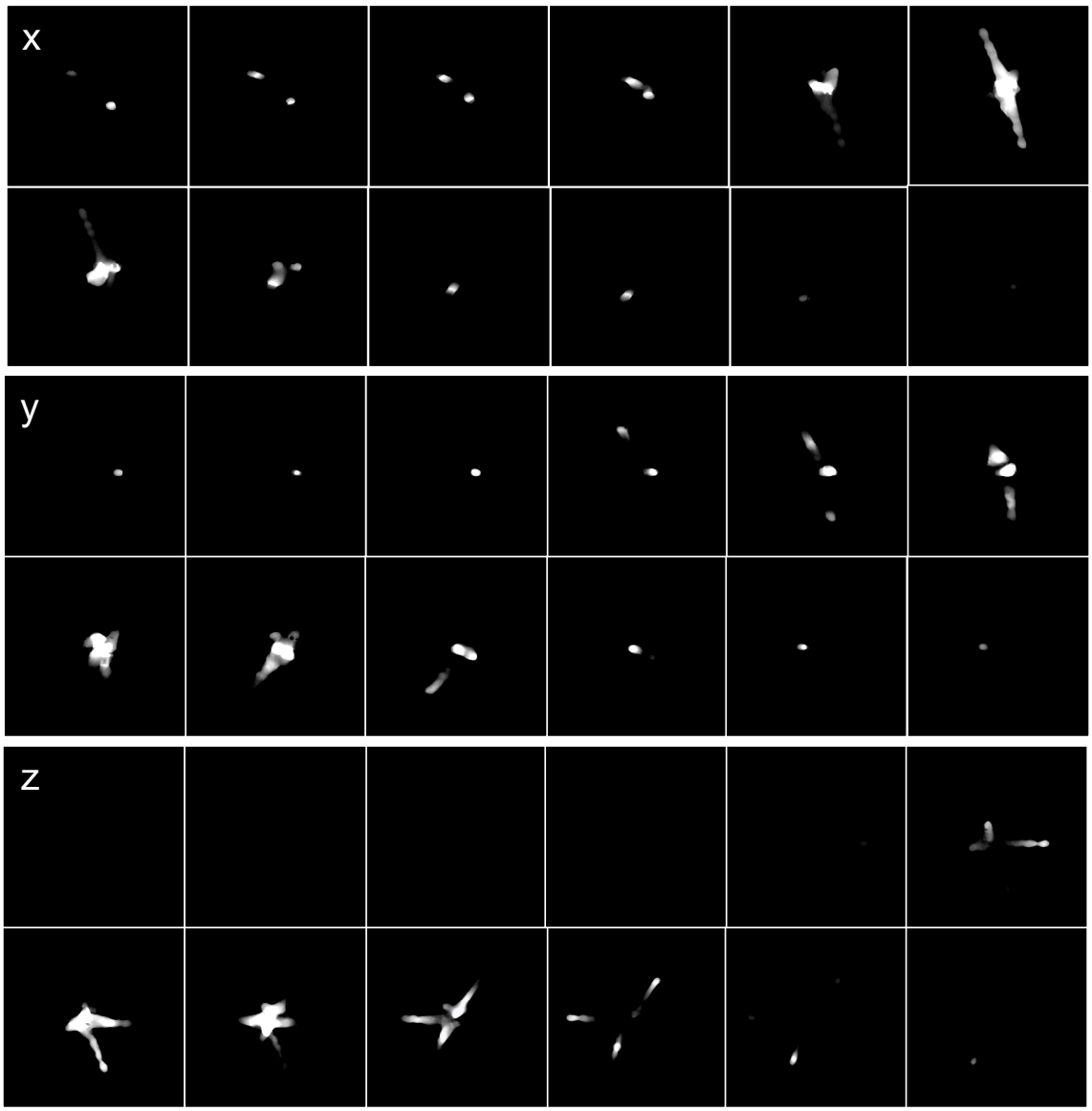

Figure S5. The quality of the tomographic reconstruction can be assessed by examining ortho slices of the reconstructed tomogram. Ortho slices in x, y, and z directions for the reconstructed nanostar reported in Figure 3 are reported here. Depth resolution: 50 nm.

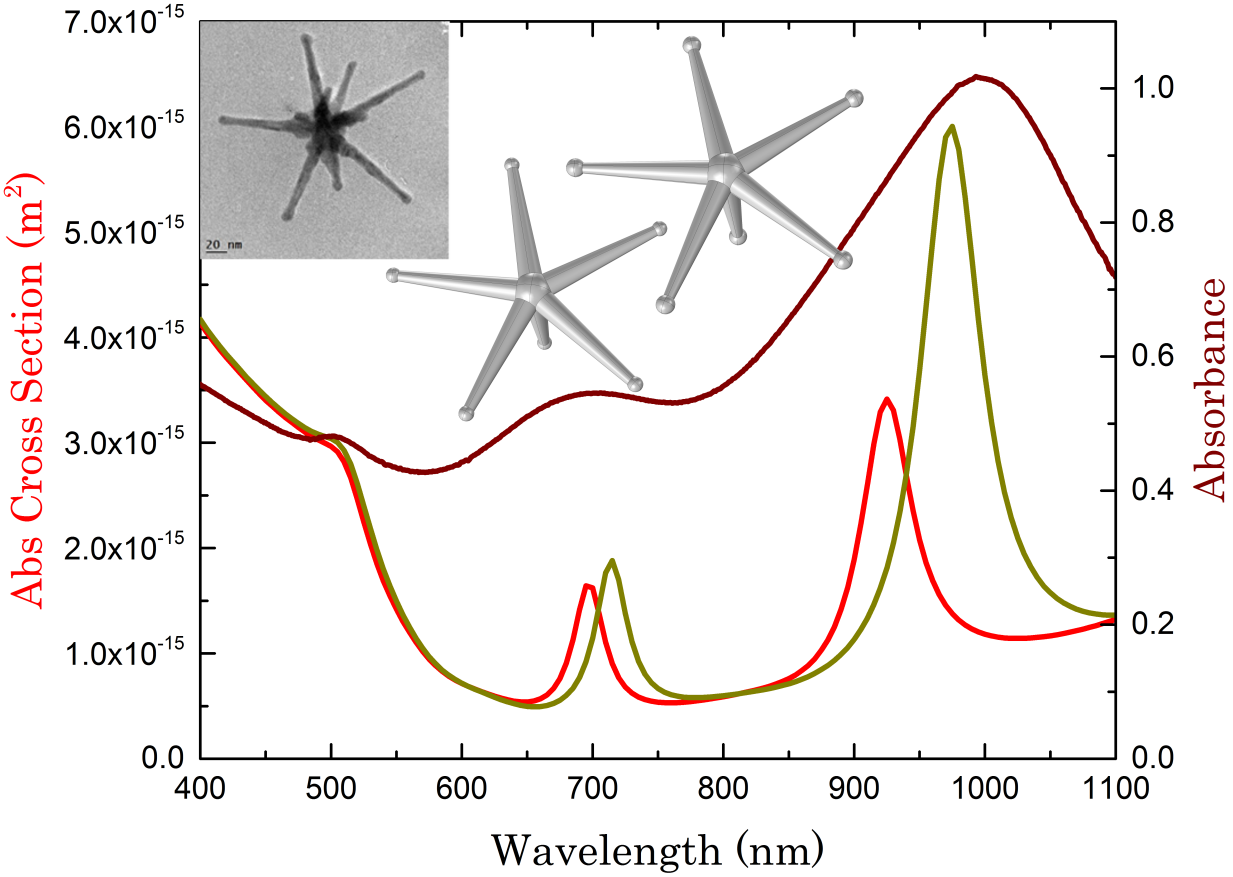

Figure S6. Juxtaposition of the experimental absorption spectrum collected on a suspension of nanostars with 100 nm spike length (TEM micrograph in inset) and two theoretical absorption cross section spectra calculated to model the optical response of nanostars characterized by spikes of slightly different aspect ratios, as defined in the main text (0.5 and 0.45 respectively). The resulting theoretical spectra exhibit notable shifts both for the second (at ca. 1000 nm) and the third (at ca. 700 nm) harmonic modes, while no shift is observed in the case of the spherical mode (at ca. 520 nm). Given that the two theoretical spectra were calculated to model individual nanostars while the experimental spectrum was collected on an ensemble of approximately 10^{14} nanostars suspended in aqueous medium, the peak broadening observed experimentally can be safely assigned to only slight differences in nanostar morphology within a batch. The good agreement between theory and experiment confirms not only the validity of our model but also the monodispersity achievable with our synthetic approach.

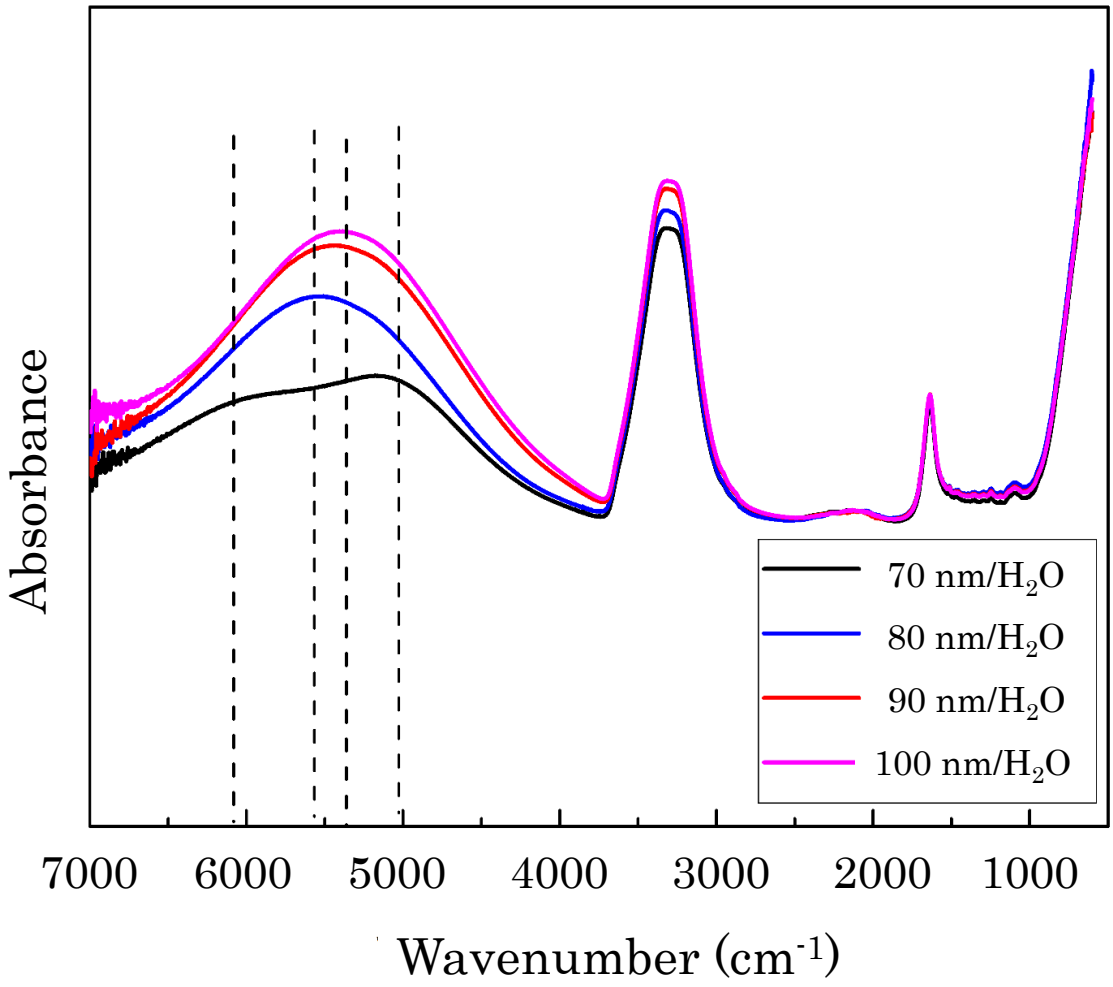

Figure S7. ATR-FTIR spectra of highly concentrated aqueous dispersions of gold nanostars with spike lengths spanning between 70 nm and 100 nm. Full spectral range, 700-7500 cm^{-1}.

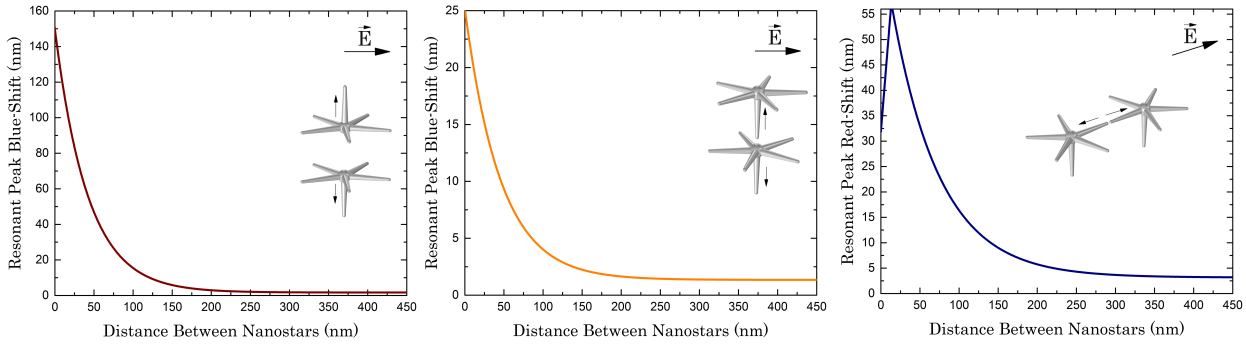

Figure S8. Quantification of the plasmonic shifts for the resonant first harmonic peak in the case of coupling of two nanostars under three different configurations. The distance in every case is defined as the physical separation between the metallic surfaces of the two adjacent nanostars. The first two configurations from the left resulted in blue-shifts, while the third resulted in a redshift that reverts at ca. 14 nm. The behavior observed for the first two configurations can be in first approximation explained by drawing a parallel to two nanorods coupling side-by-side. The behavior observed for the third configuration requires more insight. The linear region corresponds to the first few nanometers of separation between the tips coupling tip-to-tip. Within this region, because the first harmonic mode of the scattered enhanced field of the first nanostar reaches far enough to enter in resonance with the field localized at the core of the adjacent one, a strong resonance and a red-shift occur leading to an optimal coupling at ca. 14 nm. Beyond 14 nm of tip-to-tip separation the effect is reversed, as the coupling between the cores and the spikes of the adjacent nanostars weakens leading only the tips to interact, similar to two nanorods coupling tip-to-tip. Modeling of the interactions for various configurations and separation, allows us to better interpret the FTIR data and compare these results to the theoretical predictions and the Vis-NIR spectra. ATR-FTIR data were in fact collected at higher sample concentration than the Vis-NIR experiments, thus likely bringing the nanostars in close proximity to each other and, possibly, leading them to couple.

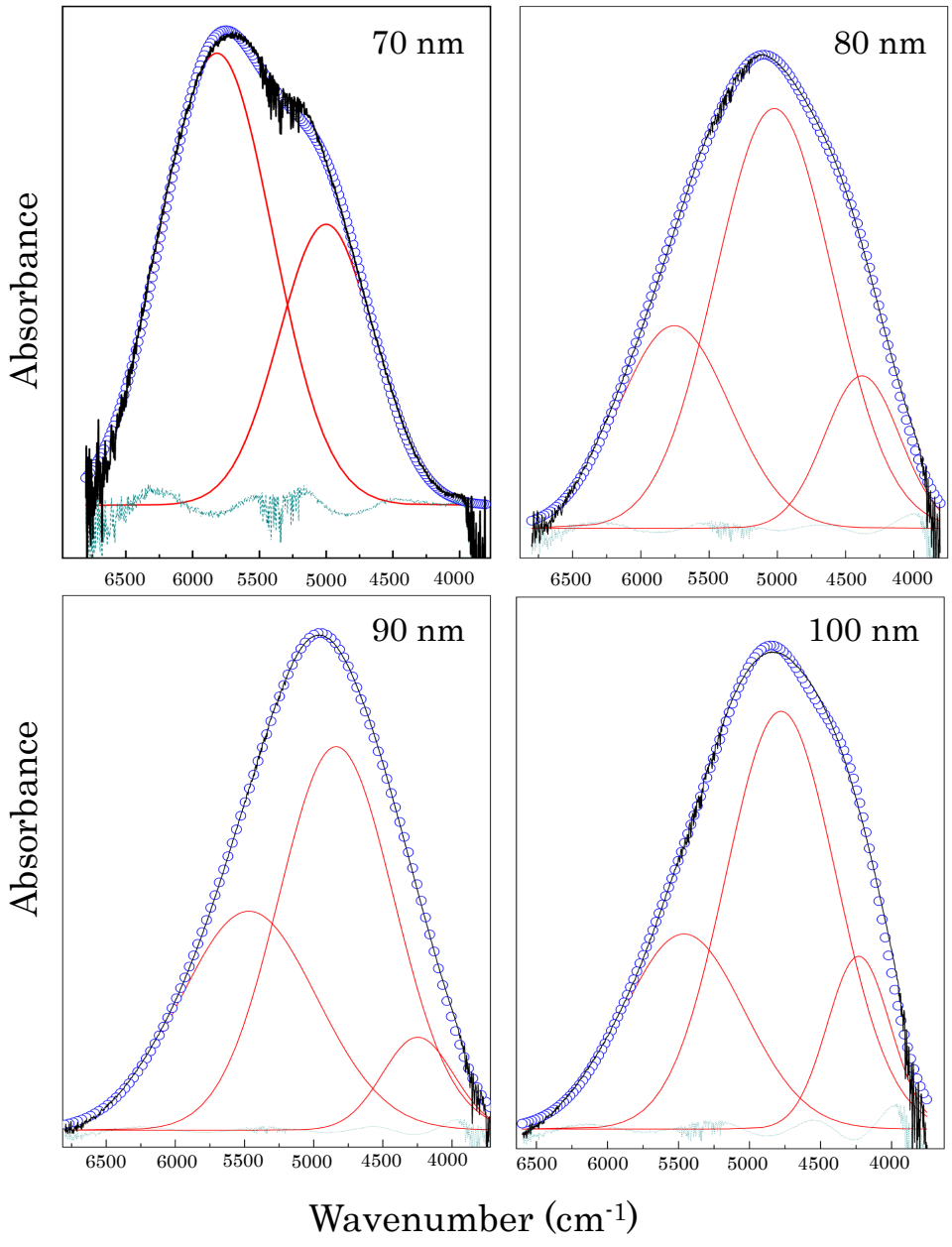

Figure S9. ATR-FTIR peak deconvolution carried out using Gauss functions based on the Levenberg–Marquardt algorithm. The error bars used in Figure 5d) were determined as the spectral distances between the experimentally determined peak maxima and the most intense of the peaks used for the deconvolution of each of the four spike-length cases.

References

1. Hale GM, Querry MR. Optical Constants of Water in the 200-nm to 200-μm Wavelength Region. *Appl Opt* 1973, **12**(3)**:** 555-563.

2. Johnson PB, Christy RW. Optical Constants of the Noble Metals. *Physical Review B* 1972, **6**(12)**:** 4370-4379.

3. Tsoulos TV, Han L, Weir J, Xin HL, Fabris L. A closer look at the physical and optical properties of gold nanostars: an experimental and computational study. *Nanoscale* 2017, **9**(11)**:** 3766-3773.